ON THE EFFECT OF IMPACTOR SHAPE ON CFRP SPACECRAFT STRUCTURES

Martin Schimmerohn[(1)], Erkai Watson[(1)], Nathanaël Durr[(1)], Robin Putzar[(1)], Beatriz Jilete[(2)], Stijn Lemmens [(3)]

[(1)] Fraunhofer Institute for High-Speed Dynamics, Ernst Mach-Institut, EMI, Ernst-Zermelo-Str. 4, 79104 Freiburg, Germany, martin.schimmerohn@emi.fraunhofer.de
[(2)] GMV@ESA/ESAC, Space Surveillance and Tracking Segment, ESA Space Situational Awareness Programme, Spain, beatriz.jilete@ext.esa.int
[(3)] Space Debris Office, European Space Agency (ESA/ESTEC), Keplerlaan 1, AZ Noordwijk 2201, the Netherlands, stijn.lemmens@esa.int

ABSTRACT

A sphere is not a very likely shape for space debris, nor does it represent a conservative assumption for assessing their damaging capability. Including shape effects in ballistic limit equations (BLE) is the next logical step in the evolution of impact risk analysis. We investigated shape effects for cylinders representing disks, rods, and nuggets in 20 hypervelocity impact tests and more than 180 numerical simulations using a hybrid DEM-FEM approach. The target represented equipment placed behind the CFRP panel structure inside a satellite. A BLE model was derived that allowed to assess the effect of non-spherical impactor shapes on spacecraft system level. Applied in the risk analysis tool PIRAT, the model manifested that the failure fluxes are significantly higher when effects of impactor shape are considered.

1 INTRODUCTION

The motivation of impact risk analyses is the prevention of space debris generating events on orbit. This includes 1) collisions with larger debris leading to breakup of the spacecraft, and 2) impact induced failure of spacecraft functions that are needed for a safe disposal at mission end (thus increasing the probability of the first risk).

Ballistic limit equations are the core for assessing impact induced failures in the risk analysis process that has been established in international standards and guidelines [1]-[3]. A typical ballistic limit equation defines a threshold particle size as a function impactor velocity and angle and the configuration of the impacted spacecraft component. Graphically represented as curve in the two-dimensional space of projectile size and impact velocity, the ballistic limit curve demarcates critical impact conditions that would lead a shield or component to fail or not to fail. The database for deriving a BLE curve is provided by hypervelocity impact experiments. Experiments are performed to constantly refine BLEs and extend their validity to include new materials and component failure. The vast majority of these experiments have been performed using spherical projectiles only.

Previous experiments and simulations with non-spherical impactors clearly indicate a higher penetrating capability compared to mass-equivalent spheres [4]-[11]. This can be related to the shock geometry and resulting fragment cloud shapes. Particularly, higher effective lengths of elongated projectiles seem to result in a focusing of ejecta mass along the impact axis. This leads to a lower spread of ejecta and higher penetration capability as the standoff distance in double wall configurations becomes less effective compared to spherical impactors.

The use of spherical projectiles embraces a practical nature, both in respect of testing and modelling. Hypervelocity impact experimentations using spheres is well established. Testing with non-spherical shapes typically involves considerable technical development effort. Including shapes in the impact analysis opens a wider parameter space as the impact behavior of a non-spherical impactor is determined not only by its shape but also by the orientation it has at impact.

Results of experimental and numerical simulation of non-spherical impactor shapes have been included in only few ballistic limit equations, often neglecting orientation and obliquity. The first systematic approach was conducted at Fraunhofer EMI using ellipsoid projectiles [12]-[13]. They introduced a shape factor to extend the spherical ballistic limit curve to a critical area of shape-dependent failures. Other works derive an orientation-averaged ballistic limit equation by including the likelihood the different impactor orientations [14]-[15]. In a systematic effort recently undertaken by NASA, Whipple shields were investigated for cylinder impacts under varied orientations [16]-[17].

ESA continued this effort in a current study with a focus on investigating the effects that non-spherical impactors have on the impact risk analysis for satellites. In this paper, we present the results of this study whose objectives were to 1) perform experiments and numerical simulations, 2) derive a non-spherical BLE model, and 3) apply this model in a test case to evaluate the effect on the risk analysis outcome.

Proc. 9th European Conference on Space Debris, Bonn, Germany, 1–4 April 2025, published by the ESA Space Debris Office
Editors: S. Lemmens, T. Flohrer & F. Schmitz, (http://conference.sdo.esoc.esa.int, April 2025)

2 EXPERIMENTS

Laboratory impact experiments have been performed using Fraunhofer EMI's caliber 8 mm light-gas gun, referred to as "Space Gun". The Space Gun derives its names from numerous and comprehensive hypervelocity impact test campaigns in the context of space debris research.

Projectiles

Shape and density of meteoroid and space debris objects are the biggest unknowns in the particle characteristics and represent a major source of uncertainty in debris flux modelling. Due to the small size and high velocity of space debris, radar and passive optical measurements from ground are limited to a lower detection threshold of about 1 cm and only give limited information about the actual shape. Information on the non-observable space debris objects smaller than 1 cm, which represent more than 99% of the debris population [18], rely on only few indirect on-orbit detections and rare data samples of microparticles collected in the Earth's stratosphere [19]. Micrometeoroids, originating from fragmentation and disaggregation of asteroids and comets, typically have irregular shapes with cavities, multi-mineral composition and porosity. The shape and composition of space debris should resemble the source of its origin. In the risk-relevant millimeter size range, fragmentation debris from 645 confirmed fragmentation events on orbit [20] represent the dominant space debris population. Data on shapes and materials of debris fragments generated in fragmentations has been gained in ground experiments. Recent effort was done by NASA's DebriSat experiment, which aimed at expanding data from the earlier SOCIT experiment for modern-design spacecraft [21]. The most common shapes found in the DebriSat analysis of breakup fragments are rod-like debris, nugget-like debris and plate-like debris. NASA derived a cylinder classification for converting these common shape classes found in the relevant size regime. Trading-off the requirements for testability and defining a minimum number of shape parameter, a cylinder may be considered a reasonable choice. Cylinder can approximate the different shape classes as a function of its length-to-diameter ratio L/D only. Furthermore, given their manufacturability and their axis symmetry, cylinders represent a good experimental option. Realizable length-to-diameter combinations have been agreed for coordinated shape effects activities by the Inter-Agency Debris Committee. We have used these combinations as a baseline for our experiments on CFRP structures:

- Plate-like debris shapes represented by flat cylinders with $L/D = 1/5$,
- Rod-like debris shapes represented by long cylinders with $L/D = 3/1$, and
- Nugget-like debris shapes represented by compact cylinders with $L/D = 2/3$.

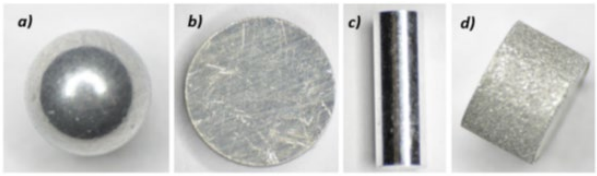

Figure 1. Sphere reference (a) and cylindrical projectiles representing disk (b), rod (c), and nugget (d).

The projectiles are made from aluminium in this study. It is the standard projectile material used in previous impact sphere projectile experiments, against which the results are compared. Aluminium represents an average density in view of 2.5 g/cm^3 average assumed for meteoroids in Grün's model and 2.8 g/cm^3 average assumed for space debris [2].

2.1 Projectile orientation

The projectile orientation plays a crucial role in the impact performance of non-spherical impactors. For the cylinder projectiles used in the experiments, we define two angles to describe their orientation upon impact:

- the angle of attack α defines the angle between projectile's symmetry axis and the impact axis,
- the roll angle β defines the angle of the plane defined by symmetry axis and impact axis to the target local system.

The roll angle is only relevant for oblique impacts, i.e. when the surface normal of the target component is inclined against the impact axis.

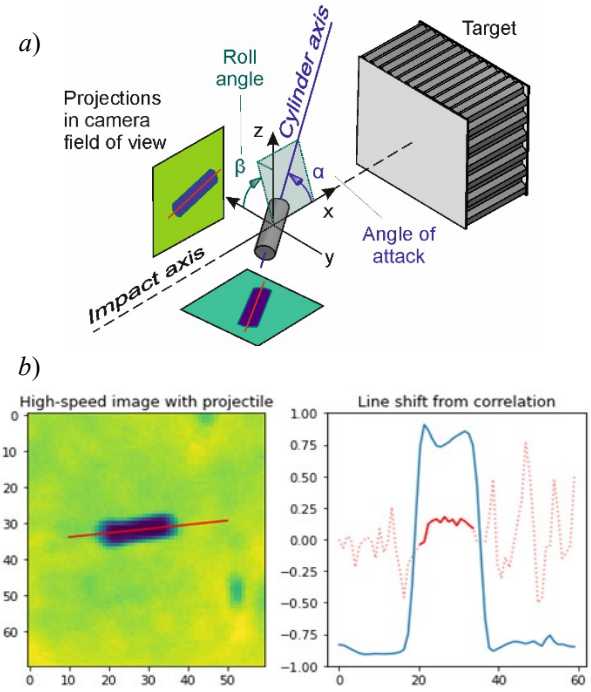

Figure 2. Projectile orientation: a) Definition of angle of attack and roll angle with respect to target. b) in-flight detection through image analysis.

Detecting the projectile orientation in flight is done by high-speed imaging from two different view angles along the impact axis. We use two cameras as shown in Fig. 2. The projection angle in both image views is then performing a line-by-line image correlation. All lines with a significant contrast shift are averaged and converted into an angle. By comparing the horizontal and vertical projecting angles and accurately know the camera and mirror orientation, the angle of attack and the roll angle of the cylinders prior to impact can be derived.

2.2 Setup

The target consisted of a CFRP sandwich panel with aluminum honeycomb core followed by a witness plate with a standoff distance of 30 cm, as shown in Fig. 3*b*). This setup reproduces an internal spacecraft equipment failure with the witness plate representing the equipment wall thickness. The equipment failure is expected for a perforation of this wall by the fragment cloud resulting from the full perforation of the outer spacecraft structure.

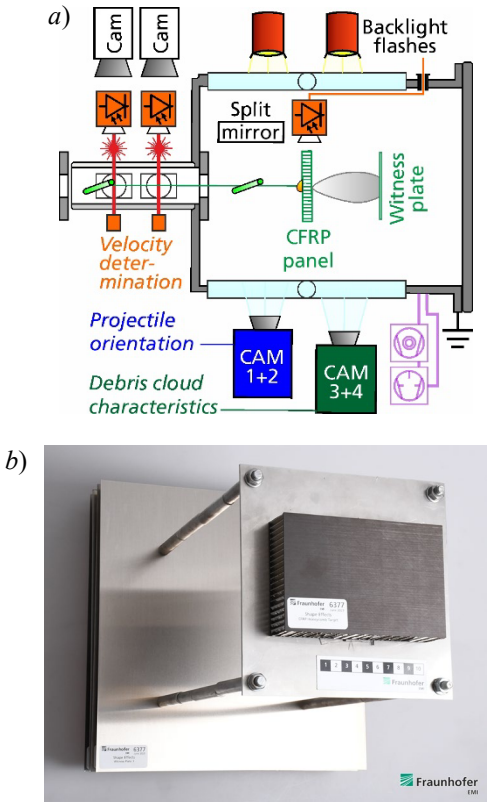

Figure 3. Experimental setup: a) Test instrumentation with high-speed cameras, b) CFRP honeycomb panel with aluminium witness plate in 30 cm standoff.

Four high-speed cameras were employed, two of each in a synchronized stereo setup. The field of view of the first two cameras captured the projectile arrival (and uprange ejecta) in front of the target to determine the projectile orientation as described above. The other two cameras observed the down-range area between the CFRP rear face sheet and the first witness plate. The experiments are backlit creating a shadowgraph of the fragment cloud. It was originally planned to used 3D particle tracking to characterize the fragment cloud for calibrating numerical simulations. While we succeeded in reconstructing the position of larger fragments at different velocities, a full quantitative cloud reconstruction was prevented by large amounts of dust fragments from the CFRP material, which complicated the image analysis.

2.3 Test Results

We performed a total of twenty hypervelocity impact experiments to evaluate the effect of projectile shape and orientation on the CFRP target setup. Exemplary test results are summarized in Tab. 1 for each shape as an overview. The projectile sizes were chosen with the goal of achieving both perforation and non-perforations of the aluminum witness plate behind the CFRP panel to accurately determine the ballistic limit, i.e. the critical diameter to induce component failure.

Table 1. Experimental results for selected tests at 0°.

Shape	Diam [mm]	Length [mm]	Mass [mg]	Vel. [km/s]	α [°]	β [°]	Fail [y/n]
Sphere	3.0	-	37.1	6.52	-	-	yes
Disk	5.0	1.0	54.3	6.48	70	-50	yes
Rod	1.8	5.4	38.6	5.37	35	40	yes
Nugget	3.8	2.5	82.2	6.27	4	-145	no

High-speed images and target photographs for the four selected experiments are presented in Fig. 4. It shows three snapshots from the video sequence for each projectile shape *a*) short before impact in front of the CFRP panel, as well as *b*) 35 µs (fast projectile fragments) and *c*) 620 µs (slow CFRP fragments) after impact between the CFRP panel and the witness plate. The projectile shape and the impact direction is indicated. The fastest fragments leading to relevant witness plate damage are identified in red in *b*).

The effect of the hypervelocity impact on the target setup is presented for the CFRP panels and the witness plates separately. The rear sides of the CFRP panels in *d*) show the visible hole and CFRP delamination damages. The weight loss of the CFRP panel Δm_{CFRP} was quantified and is given along with the kinetic energy of the projectile E_{imp}. The damage on the front sides of the witness plates *e*) show the number of holes N_h or the onset of incipient or detached spall. This damage is quantified for deriving the ballistic limit. The origin of the fragments causing the impact damage is revealed by the color differences. Damages caused by aluminum projectile fragments appear whitish/silvery, while the CFRP fragments leave dark marks on the witness plate. All observed witness plate perforations were caused by fast aluminum fragments.

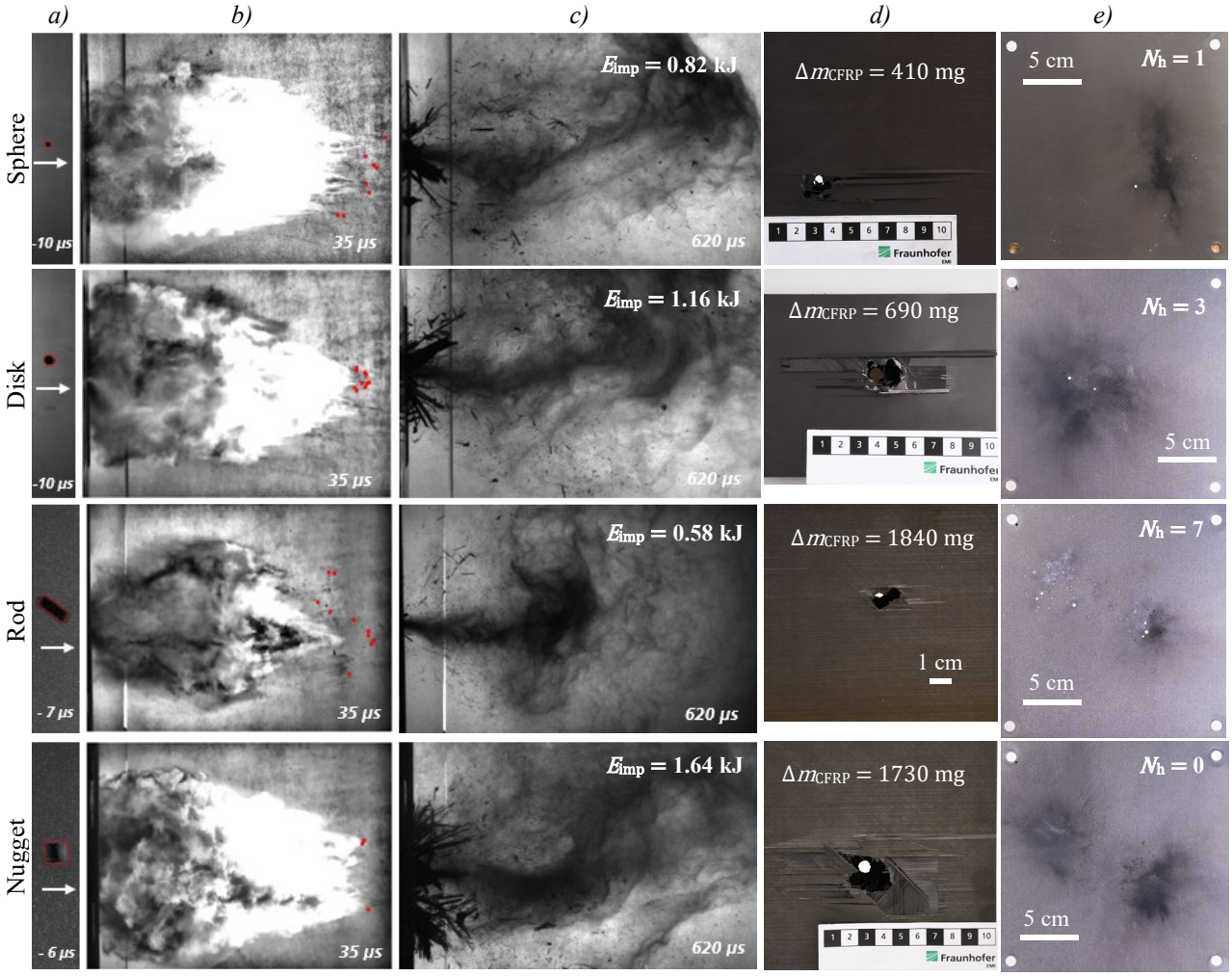

Figure 4. Hypervelocity impact experiment results for each shape (cf. Tab. 1): a) Impactor microseconds before impact, b) debris fragment cloud 35 µs after impact with larger fast fragments highlighted in red, c) fragment cloud with slow CFRP fragments 620 µs after impact with projectile's kinetic energy E_{imp}, d) CFRP panel rear side damage with measured mass loss Δm_{CFRP}, e) witness plate damage with number of clear perforations N_h.

Comparing the cylinder impactor damages to the sphere ballistic limit reference (I) shows that the rod caused the maximum damage to both target components with the highest mass removed from the CFRP panel and seven clear perforations on the witness plate. The nugget, although it had the highest mass and impact energy, induced a greater loss of mass in the CFRP panel than the sphere and disk, but did not perforate the sheet and thus remains below the ballistic limit.

The disk projectile, impacting with an edge first, caused less damage compared to the rod and more damage than the sphere but had a higher impact energy than both. It is apparent that the presented experimental results only cover a part of the vast parameter space opened up by including projectile shapes and orientation. For each shape, a systematic variation of the orientation at impact is required, which is not fully accessible in experiments with reasonable effort. This makes numerical simulation an essential part of shape effect research.

3 SIMULATIONS

We extensively used numerical simulations to extend the parameter space by 1) sampling different orientations of the tested cylinders, 2) including oblique impacts, 3) varying velocity, and 4) investigating more extreme length-to-width aspect ratio of the cylinder projectiles.

3.1 Method

The target setup consisting of a CFRP structure wall and a witness plate in a relatively large distance makes the simulations using standard methods and tools quite demanding in terms of fidelity and computational effort. For realizing a high number of simulations with stable and accurate predictions, we applied a two-part simulation approach, where a discrete element method is used to model the fragmentation of the impactor upon contact with the CFRP sandwich panel, followed by a

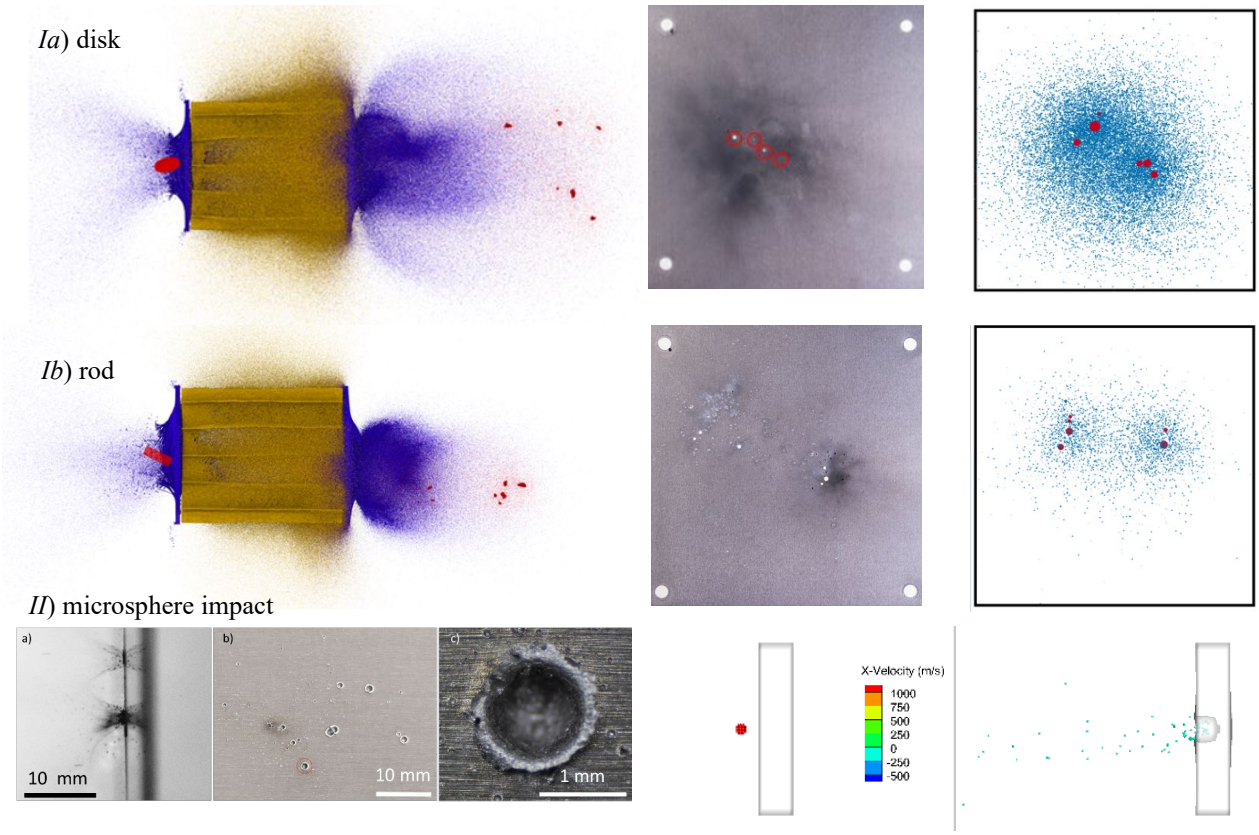

Figure 5. Calibration of numerical simulations: I) show MD-CUBE simulation of the disk (a) and rod (b) experiments, respectively (cf. Fig. 4 and Tab. 1). The witness plate damages are compared to the experimental results. II) Impact experiments with 300 µm glass spheres on the witness plate for calibrating the failure strain settings for SOPHIA.

finite element modeling of the perforation and cratering of the aluminum witness plate. This combination allows each simulation approach to be applied under conditions where it performs best.

The first part of the impact process, the hypervelocity impact of an aluminum cylinder with the CFRP panel, is dominated by fragmentation and is performed with Fraunhofer EMI's discrete element method (DEM) program MD-CUBE [22]-[23]. This tool is able to accurately simulate the creation of individual fragments in HVI debris clouds in aluminum and CFRP [24].

The second part of the impact process, the interaction of the resulting debris cloud fragments with the witness plate, is dominated by material strength, and is performed with an explicit finite element method (FEM), which is more suited for predicting the failure of the witness plate. Here we used Fraunhofer EMI's hydrocode SOPHIA [25]-[26].

The coupling of the two methods is achieved by importing the debris cloud fragments from MD-CUBE into the SOPHIA. Each fragment from MD-CUBE, consisting of multiple particles, is converted into mass points used in SOPHIA. To reduce the computational effort due to the distance between the fragment cloud emerging from the sandwich structure and the witness plate, the trajectory of each fragment is extrapolated until the fastest fragment are just in front of the witness plate.

The witness plate is modelled with a finite element mesh and, unlike MD-CUBE, can be provided with a plasticity model and an equation of state into which conventional aluminum parameters can be incorporated. A simple but robust erosion criterion is used to model the perforation by defining a critical failure strain. The interaction between the mass points of the fragment cloud and the finite element mesh of the witness plate is modelled using a proven contact method.

3.2 Calibration

The two-step approach allowed us to calibrate and validate the DEM model and the FEM model independently. Instead of validating the final result of the simulation based solely on the pass/fail criteria of the witness plate, we are able to attain a more nuanced picture for both parts of the simulation chain.

The DEM model was calibrated using the experimental data. Since the particle tracking was impaired by the darkening of CFRP dust, the craters and perforation damages on the witness plate provided quantitative data to evaluate the spatial size and velocity distribution of the debris cloud [27]. Fig. 5*a-b*) shows the example of the

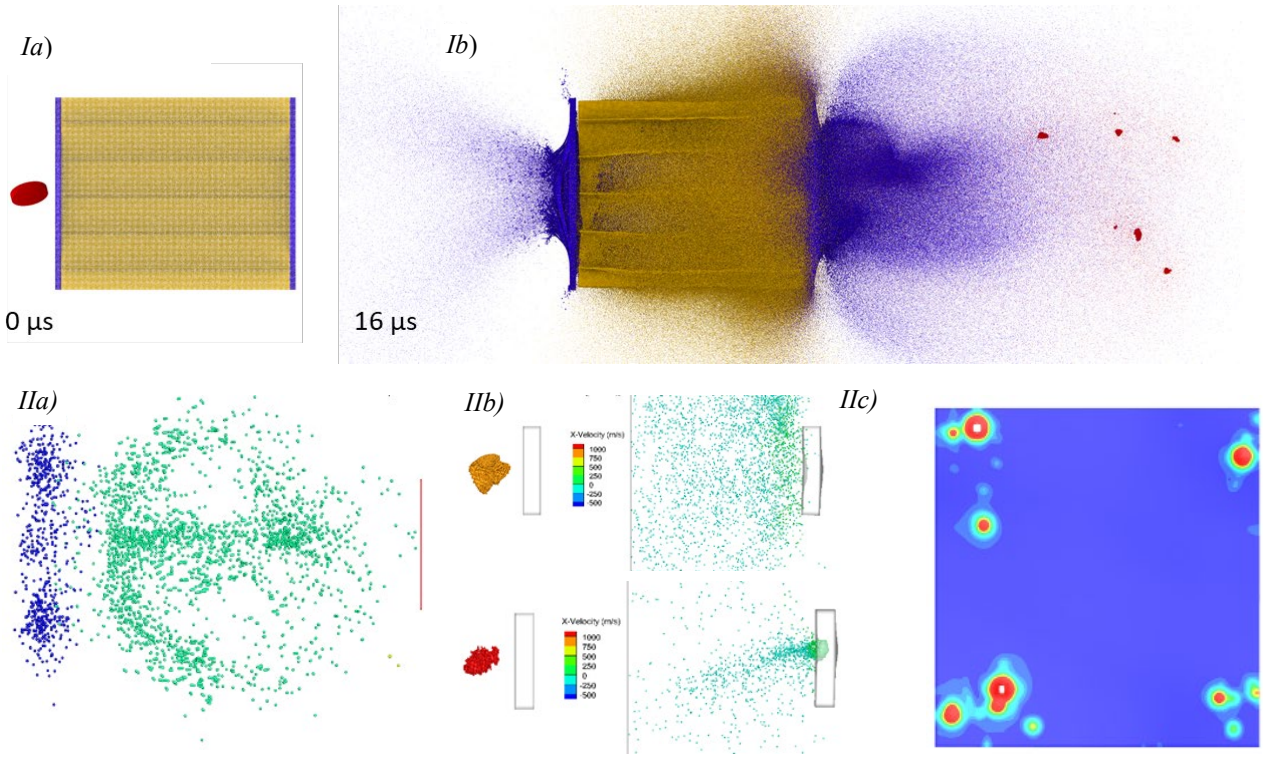

Figure 6. Numerical simulation. I) MD-CUBE simulation of an aluminum disk (red) impacting a CFRP sandwich panel (yellow for Al honeycomb, blue for CFRP) prior to impact (a) and after perforation (b) of the CFRP panel. II) SOPHIA simulation for the same virtual experiment showing (a) the transferred fragment cloud prior to impact, (b) individual fragment impacts on the witness plates, and (c) computed witness plate damages.

disk and rod impact presented above. Shown are snapshots of the fragment clouds in the MD-CUBE simulations along with a comparison of the experiment and virtual witness plate.

The FEM part of the simulation was calibrated by performing an impact experiment on a witness plate. We used 300 µm glass spheres, which are of a similar density, size, and velocity as the fragments causing penetrations in the experiments. The failure strain of the FEM model was adjusted until the simulative crater depth matches the experimental one, cf. Fig. 5*c*).

3.3 Simulation Results

Over 180 numerical simulations were performed for the CFRP target setup. Fig. 6 gives an example of a disk impact with a) showing the approach to and the perforation of the CFRP panel simulated using MD-CUBE. The SOPHIA simulation is shown in b) with the cloud of fragments (having relevant size to cause damage) prior to impact on the witness plate and the top view on the damages generated on it after impact.

4 MODELLING

Data from both experiments and numerical simulations was used to derive a prototype model suitable for implementation in risk analysis tools. Today, all relevant engineering tools applied for impact risk analysis rely on ballistic limit equations, so the motivation was to keep a similar form to ensure compatibility.

In the first step, the impactor size threshold for perforation of the witness plate was determined based on both experimental and numerical data. In the second step, geometric parameters were derived for the projectiles using both projectile shape and orientation. Those parameters are generic in the sense that they are in principle derivable for all shapes and include (i.e. are dependent on) the impact orientation of a particle. In the third step, the geometric parameters were correlated to the available impact data to find a suitable model. In the fourth step, the model was applied to all available data.

The details of the prototype model will be subject of another publication. In this overview paper, we instead present a graph of the applied model in Fig 7. It shows the model curves along with experimental and simulation data at 6 km/s for the tested cylinder aspect ratios plus one with $L/D = 1/1$. The model outputs a spherical ballistic limit diameter, which represents the size of a sphere that causes the same damage as the cylindrical impactors. Expressed as mass equivalent sphere size D_{sph}, this diameter can then be compared to the ballistic limit size D_{bl} as predicted by standard ballistic limit equations. The model parameters are the angle of attack and the length and diameter of the right circular cylinder.

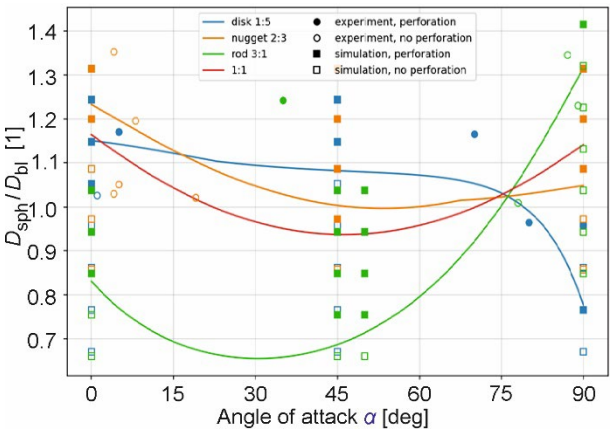

Figure 7. Shape effect model for comparing the ballistic limit diameter of a mass equivalent sphere D_{sph} with the classic ballistic limit D_{bl} for the investigated CFRP setup for different L/D and α.

The equivalent size threshold is based on equivalent mass considerations and the projected cross section area on the target surface. The comparison to the test data in Fig. 7 shows an overall good agreement to demarcate fail from no fail conditions, with a low tendency of overprediction for nuggets and discs at low α. For combinations where $D_{sph}/D_{bl} \leq 1$ is fulfilled, the shape effect leads to a lower ballistic limit, i.e. the vulnerability to the cylinder shape is higher compared to a sphere.

5 TEST CASE EVALUATION

The overarching goal of this shape effect research is to quantify the consequences of including shape in the impact risk analysis at system level. For this purpose, we performed an exemplary risk assessment using the new shape effects model and a simplified test case.

5.1 Shape and Orientation Distribution

Applying the shape effects model found in this work is straightforward if the cylinder sizes L and D and the angle of attack α are known for the impactors. However, such shape and orientation parameters are not included in the current space debris environment models. Therefore, we derived probability density functions for incorporating these parameters under the following assumptions:

- All orientations occur with the same likelihood with the probability density function for the angle of attack is $P[\alpha] = \sin[\alpha]$.
- L/D distribution of impactors resembles the shape distribution found in breakup tests.

For the latter, recently published L/D distributions for the DebriSat impact experiment have been used [28]. This includes distributions of the L/D ratio of the SOCIT test fragments as well as the DebriSat test with and without CFRP fragments included. The resulting probability density functions are shown in Fig 8.

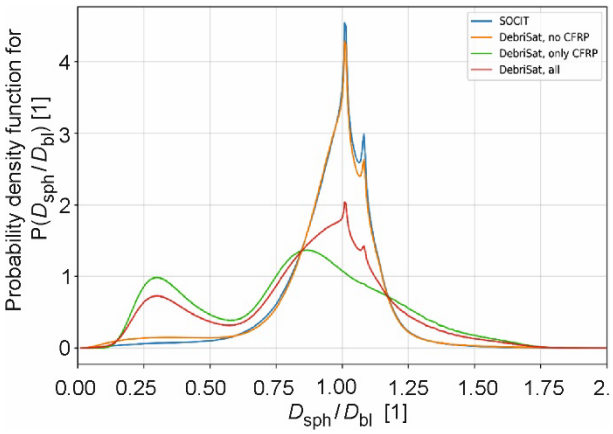

Figure 8. Probability density functions as derived for for L/D distributions found in SOCIT and DebriSat ground tests (no, w/, and w/o CFRP fragments).

5.2 Test Case Definition

A simplified generic spacecraft geometry is used for the risk analysis. The geometry reflects the test cases defined for internal component failure tests in the Protection Manual (Version 7.2) of the Inter-Agency Debris Coordination Committee [3]. It consists of a generic benchmark configuration used for inter-calibration of risk analysis tools as shown in Fig 9.

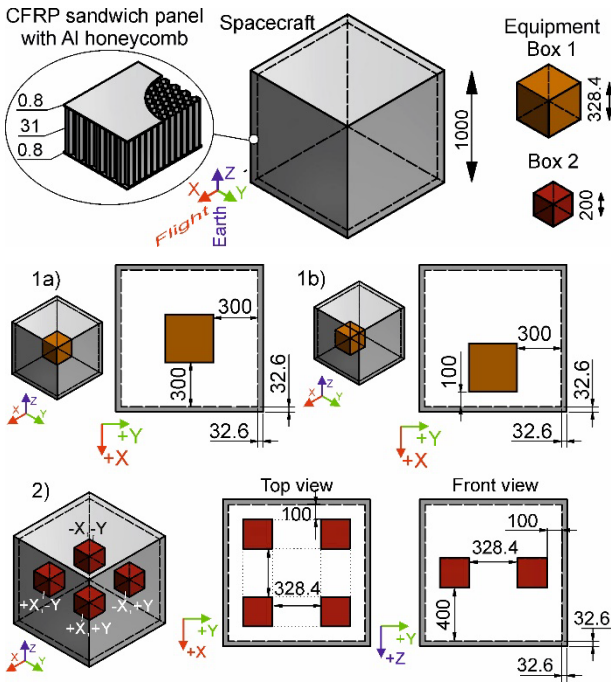

Figure 9. Test case definition reflecting the benchmark cases for internal equipment failure of the IADC Protection Manual [3].

An internal component box with 1 mm thick wall is positioned inside a cube-shaped outer satellite hull made from CFRP sandwich panels. It is not by coincidence that

this test case corresponds to the tested setup of this study. For the spherical impactor reference, the SRL ballistic limit equations can be applied for both the CFRP honeycomb panel perforation and the complete set-up including the witness plate [29], [30].

We used Fraunhofer EMI's risk analysis tool PIRAT for the impact risk assessment, which supports 3D models and includes internal component damage analysis [31]. For this test case evaluation, we interfaced with the MASTER-8 flux model for a LEO (720 km, SSO) and a GEO scenario.

5.3 Risk Analysis Results

The results of the test case evaluation are overviewed in Tab. 2 for the perforations of the CFRP panel outer hull. We present only the total failure fluxes summed over the six faces of the spacecraft. The factor gives the relative deviation from the spherical reference.

Table 2. Test case analysis results for the CFRP panel perforation for spherical and cylinder shapes using different L/D distributions.

Orbit		L/D distribution	Total failure flux	Deviation factor
LEO	Sphere		1.02E+02	-
	Shape	SOCIT	1.97E+02	1.94
		DebriSat all	5.10E+02	4.02
		DebriSat no CFRP	2.69E+02	1.65
GEO	Sphere		1.38E-03	-
	Shape	SOCIT	3.54E-02	1.94
		DebriSat all	1.30E-01	4.02
		DebriSat no CFRP	8.87E-02	1.65

The overall picture is that cylindrical particles lead to significantly more CFRP sandwich panel perforations than spherical particles. The variation is relatively high for different surfaces, indicating a potential velocity influence. The same applies for the GEO case, for which the deviations particularly in flight direction are the highest. However, it should be noted that the experiments have been performed mostly at velocities around 6 km/s. Furthermore, the simulations are calibrated for a reproducing both the fragment cloud behind the panel and the witness damage, but not the CFRP panel perforations itself. The results for the outer hull perforations should be therefore treated with care unless more investigation on the ballistic limit of the CFRP panel have been performed for shaped impactors.

The failure counts for the internal component damages, the test scenario on which the investigation and model development is based, are presented in Tab. 3. The deviation factors for the different test cases over all surfaces is at least four times higher compared to the spherical impactors.

Table 3. Test case analysis results for failures of internal equipment behind CFRP panels normalized to spherical BLE analysis results.

Orbit	L/D distribution	Test case (se Fig. 9)	Deviation factor
LEO	SOCIT	1a	10.6
		1b	14.2
		2/+X +Y	19.9
		2/-X -Y	8.1
	DebriSat all	1a	13.0
		1b	19.3
		2/+X +Y	39.6
		2/-X -Y	10.1
	DebriSat no CFRP	1a	30.3
		1b	40.7
		2/+X +Y	56.3
		2/-X -Y	23.0
LEO	SOCIT	1a	17.9
		1b	17.2
		2/+X +Y	17.8
		2/-X -Y	20.7
	DebriSat all	1a	19.2
		1b	18.4
		2/+X +Y	18.5
		2/-X -Y	22.2
	DebriSat no CFRP	1a	50.2
		1b	48.3
		2/+X +Y	50.1
		2/-X -Y	58.0

Interestingly, the discrepancy is highest for the DebriSat L/D distributions without CFRP, which has a much lower amount of rod and disk like impactors. Though these can be considerably more penetrative, but only in a limited range of potential orientations.

The conversion metric of the equivalent sphere size may introduce a bias in the flux determination. The new shape effect model calculates the diameter of a mass-equivalent sphere through assuming equivalent volume. The characteristic length definition used in the breakup experiments yields smaller equivalent sphere sizes for compact cylinders for $0.3 \leq L/D < 3$ and larger sphere sizes for more extreme L/D. However, the deviation factor is < 3 for the considered aspect ratios. Thus, the tendency to higher failure fluxes for shaped impactors does not change. Overall, there is a strong indication that including the shape of impactors significantly increases the vulnerability to space debris impacts for internal spacecraft components.

6 CONCLUSIONS

We accomplished the first systematic study on impactor shape effects for internal equipment behind spacecraft structure walls. Different impactor shapes were realized

in experiments by varying the length-to-diameter ratio of aluminum right cylinders to represent disks ($L/D = 1/5$), rods ($L/D = 3/1$), and nuggets ($L/D = 2/3$) as found in the DebriSat experiment. Results of numerical simulations using a combined DEM-FEM approach complemented the comprehensive test database for the wide parameter space opened to include shapes and their orientation at impact.

A prototype model was derived that calculates an equivalent spherical ballistic limit D_{sbl} for the shaped impactors as function of their length-to-diameter ratio and the angle of attack. Comparing D_{sbl} to the ballistic limit diameter of a standard ballistic limit equation of spherical impactors allows to assess the criticality of including the space debris shape. The model indicates that including shapes leads to lower critical diameter compared to the standard models based on data for spherical impactors, i.e. the current spherical standard model in use is non-conservative for the tested configuration. Given the wider parameter space, there is a higher variation depending on the impactor orientation at impact. A risk analysis was performed for a generalized benchmark case with internal equipment boxes behind CFRP sandwich panel walls. For averaged angle of attacks and L/D distributions as found in ground experiments, the risk analysis showed significantly higher failure rates when shape effects are considered.

As it is true for all risk assessments based on ballistic limit equations, the derived model validity is limited to the tested configuration. We currently perform more tests and simulations for the presented CFRP multi-shock shield using different projectile material densities. The aim of this effort is to more accurately reflect shape and density effects of the actual space debris objects. A better understanding of the hypervelocity impact response to varied impactor characteristics can improve the accuracy of failure predictions in risk analysis for safe and sustainable space operations.

7 ACKNOWLEDGEMENTS

The work described herein was partially carried out under a program funded by the European Space Agency under the project S2P S1-SC-05 Shape Effect Modelling for Risk Evaluation, Contract No. 4000136979/22/D/MRP.

8 REFERENCES

1. ISO 16126:2024, Space systems — Survivability of unmanned spacecraft against space debris and meteoroid impacts for the purpose of space debris mitigation.
2. ECSS-E-ST-10-04C, Space Engineering – Space Environment, Rev. 1, 15 June 2020.
3. Inter-agency Space Debris Coordination Committee, Protection Manual, IADC-04-03, Version 7.1, 2018.
4. Gehring, J.W. (1970). Engineering considerations in hypervelocity impact. *High-velocity impact phenomena*. Elsevier, Chapter 9, 463–514.
5. Morrison, R.H. (1972). *Investigation of Projectile Shape Effects in Hypervelocity Impact of a Double-Sheet Structure*. NASA Technical Note D-6944.
6. Piekutowski, A.J. (1987). Debris clouds generated by hypervelocity impact of cylindrical projectiles with thin aluminum plates. *Int. J. Impact Eng.* **5** (1-4), 509-518.
7. Konrad, C.H., Chhabildas, L.C., Boslough, M.B. et al. (1994). *Dependence of debris cloud formation on projectile shape*. AIP Conf. Proc. 309, 1845-1848.
8. Hu, K. & Schonberg, W.P. (2003). Ballistic Limit Curves for Non-Spherical Projectiles Impacting Dual-Wall Systems. *Int. J. Impact Eng.* **29**, 345-356.
9. Ioilev, A.G., Bashurov, V.V., Konyaeva, O.V. (2005). *Influence of the Hypervelocity Disk Projectile Orientation on Damage to Target: Numerical Simulation*. 4th Eur. Conf. Space Debris, ESA SP-587.
10. Williamsen, J.E., Evans, S. (2008). Predicting orbital debris shape and orientation effects on spacecraft shield ballistic limits based on characteristic length. *Int. J. Impact Eng.* **33** (1–12), 862-871.
11. Miller, J.E., Davis, B., McCandless, R. et al (2021): Experimental Hypervelocity Impacts of Non-Spherical Projectiles on Whipple Shields. *NASA Orbital Debris Quarterly News* 25 (4).
12. Schäfer, F., Herrwerth, M., Hiermaier, S.J. et al. (2001). Shape effects in hypervelocity impact on semi-infinite metallic targets. *Int. J. Impact Eng.* **26** (No. 1–10), 699-711.
13. Schäfer, F.; Hiermaier, S.; Schneider, E. (2003). *Ballistic limit equation for the normal impact of unyawed ellipsoid-shaped projectiles on aluminium Whipple Shields*. Proc. 54th IAC, IAC-03-IAA.5.3.06.
14. Schonberg, W.P & Williamsen, J.E. (2006). RCS-Based Ballistic Limit Curves for Non-Spherical Projectiles Impacting Dual-Wall Spacecraft Systems. *Int. J. Impact Eng.* **33**, 763-770.
15. Williamsen, J.E., Schonberg, W.P., Jenkin, A.B. (2011): On the Effect of Considering More Realistic Particle Shape and Mass Parameters in MMOD Risk Assessments. *Adv. Space Res.* **47**, 1006–1019.
16. Carrasquilla, M.J.; Miller, J.E. (2017). Shape Effect Analysis of Aluminum Projectile Impact on Whipple Shields. *Procedia Engineering* **204**, 308-314.
17. Miller, J.E. (2019). Considerations of oblique impacts of non-spherical, graphite-epoxy projectiles. *Proc. 1st Int. Orbital Debris Conf.*, LPI Contribution

No. 2109, id.6021.

18. Lee, C.G., Slade, M.A., Jao, J.S. et al. (2020). Micro-meteoroid and orbital debris radar from Goldstone radar observations. *J. Space Safety Eng.* **7** (3), 242-248.

19. Jessberger, E.K., Stephan, T, Rost, D. et al. (2001). Properties of interplanetary dust: information from collected samples. *Interplanetary Dust*, 253-294.

20. ESA's Annual Space Environment Report, ESA Space Debris Office, GEN-DB-LOG-00288-OPS-SD, Issue 8.0, 19 July 2024.

21. Cowardin, H., Cruz, C., Murray, J. et al. (2023). Updates on the DebriSat hypervelocity experiment and characterization of fragments in support of environmental models. *Int. J. Impact Eng.* **180**, 104669.

22. Watson, E. & Steinhauser, M. (2017). Discrete Particle Method for Simulating Hypervelocity Impact Phenomena, *Materials* **10** (4), 379

23. Watson, N. Durr, J. L. S. Murillo, M. Büttner, & P. Matura (2022). *Simulating Hypervelocity Impacts on CFRP with a Discrete Element Approach*. Proc. 16th Hypervelocity Impact Symp.

24. Watson, E. Sandoval Murillo, J.L., Durr, N. & Ledford, N. (2024). Simulating impact-induced satellite breakups with a discrete element method, *Acta Astronaut*. **219**, 428–437.

25. Schimmerohn, M., Matura, P., Watson, E. et al. (2020). Numerical investigation on the standard catastrophic breakup criteria, *Acta Astronaut*. **178**, 265–271.

26. Ganzenmüller, G.C. (2014). An Hourglass Control Algorithm for Lagrangian Smooth Particle Hydrodynamics, *Computer Methods in Appl. Mech. Eng.* 286.

27. Watson, E., Putzar, R., Durr, N. et al. (2024). *Shape Effect of Non-Spherical Projectiles on CFRP Spacecraft Structures*. 17th Hypervelocity Impact Symposium 2024.

28. Seago, J. H., Cowardin, H., Anz-Meador, P. et al. (2024). An approach to shape parameterization using laboratory hypervelocity impact experiments. *J. Space Safety Eng* **11** (3), 518-525.

29. Schäfer, F., Putzar, R., Lambert, M. (2008). Vulnerability of Satellite Equipment to Hypervelocity Impacts. *Int. J. Impact Eng.* **35** (12), 1728-1734.

30. Ryan, S., Schäfer, F., Destefanis, R. & Lambert, M. (2008). A ballistic limit equation for hypervelocity impacts on composite honeycomb sandwich panel satellite structures. *Adv. Space Res.* **41** (7), 1152-1166.

31. Gulde, M., Kempf, S., Schäfer, F. (2016). Fast and Flexible Space Debris Risk Assessment for Satellites. *J. Space Safety Eng.* **3** (3), 111-113.